Electrochimica Acta 475 (2024) 143679

Contents lists available at ScienceDirect

Electrochimica Acta

journal homepage: www.journals.elsevier.com/electrochimica-acta

One-step electrodeposited nickel phosphide electrode for pH-universal electrochemical hydrogen production

A.B. Silva, M. Medina, L.A. Goulart, L.H. Mascaro *

Universidade Federal de São Carlos, Rod. Washington Luiz, Km 235, São Carlos – SP, Brazil, 13565-905

ARTICLE INFO

Keywords:
Nickel phosphide
HER
One-step electrodeposition
pH-universal

ABSTRACT

Herein, we describe the development and study of the relationship between the Ni molar ratio of amorphous nickel phosphide (Ni-P) electrodes synthesized via electrodeposition on Ni foam (NF) applied as a non-precious electrocatalyst for the Hydrogen Evolution Reaction (HER) in a pH-universal. The 3-Ni-P electrode displayed outstanding HER performance in alkaline, neutral, and acidic conditions with an overpotential of 69, 165, and 56 mV at –10 mA cm^{-2}. Furthermore, the Ni-P films showed excellent stability under the different conditions studied. The optimized 3-Ni-P electrode performance was attributed to its granular structure with a large surface area, enabling good interaction with the electrolyte, which endorses the HER kinetics. These results are relevant concerning an adequate choice of stable catalyst material, easy to synthesize and capable of operating in a wide range of pH with high efficiency for HER.

1. Introduction

The aggravation of the environmental destruction derived from massive fossil fuel consumption evidences the urge to transform the global energy system (production, transport, and consumption)[1,2]. Hydrogen has been considered the optimal energy vector for achieving a more sustainable energy system [3]. Electrochemical hydrogen production by water electrolysis is a promising, environmentally-friendly technique to produce highly pure hydrogen (99.999 %) with zero carbon footprints. The hydrogen production efficiency depends on the electrocatalyst's ability to get through the high energy barrier required for the reaction. The state-of-the-art hydrogen evolution reaction (HER) electrocatalyst is Pt/C; however, it is high-cost, and scarcity compromises its widespread application, elevating electrolysis device costs [4,5]. Therefore, developing low-cost, non-noble metal-based materials with high activity for HER is imminent for achieving good cost-effectiveness for H_2 production.

For instance, transition metal phosphides (TMPs) are the most promising candidates for replacing Pt-group catalysts. Metal phosphide's intrinsic activity results from the P and metal atoms' negative and positive charge nature, inflicting an electronegativity difference that weakens the metal-hydrogen bond strength, stimulating H desorption and hence the HER performance [6,7]. Among the TMPs, nickel phosphides have been regarded as potential materials owing to their electronic structure and polytropic compositions. Moreover, Ni-P has also shown interesting anticorrosive features in various pH (acidic, neutral, and alkaline)[8–10]. Several approaches can be used to fabricate Ni-P-based catalysts; most require multiple steps and a phosphorization step under inert atmospheres. Hence, using the electrodeposition technique brings the advantage of working at room temperature in easy-scalable electrodes using different geometric-shaped substrates.

Moreover, electrodeposited metal phosphide electrocatalysts usually lead to the formation of amorphous films [11]. Amorphous metal phosphide films are interesting since their disordered structures possess abundant active sites for the HER. Controlling the composition of amorphous structured metal phosphide catalyst is vital to achieving an optimum catalytic response and stability. Kucernak and Sundaram [12] observed a direct correlation between P content and nickel phosphide corrosion resistance. Laursen and co-workers [13] proved that even a slow percent of P content could develop highly stable catalysts in alkaline and acidic media.

Amorphous TMPs have advantages over crystalline materials, such as the large specific surface area, and provide lower resistance in electrolyte/electrode [11,14]. Some authors [15–17] have shown promising results for electrodeposited Ni-P in acidic and alkaline electrolytes. However, a consistent study of electrodeposited Ni-P films with good performance for HER in a pH-universal range is still lacking. Most of the reported top-performing nickel phosphide HER perform well in just one

* Corresponding author.
E-mail address: lmascaro@pq.cnpq.br (L.H. Mascaro).

https://doi.org/10.1016/j.electacta.2023.143679
Received 1 August 2023; Received in revised form 9 November 2023; Accepted 16 December 2023
Available online 17 December 2023

pH range, most alkaline or acidic, while the application in neutral conditions is neglected. This work investigates the performance of electrodes based on predominantly amorphous Ni-P films constructed by one-step electrodeposition on a 3D Ni foam skeleton for HER under acidic, neutral, and alkaline electrolytes (pH-universal). The effect of the deposition bath Ni ratio on the electrodes' structure and electrocatalytic activity was investigated. The optimized electrode presented outstanding performances in the HER for all the pH ranges studied with low overpotentials for –10 and –100 mA cm^{-2}. Furthermore, the electrode presented excellent durability and stability in long-term electrolysis for harsh and neutral conditions. The results demonstrate the one-step electrodeposition method as promising to design highly efficient and stable nickel phosphide electrodes for HER in pH-universal conditions.

2. Experimental

2.1. Preparation of the Ni-P electrodes

Nickel phosphide films were synthesized via electrodeposition in a single-compartment electrochemical cell, using an $Ag_{(s)}/AgCl_{(s)}/KCl_{sat.}$ as reference and carbon rod electrodes as the counter electrode. Before electrodeposition, the Ni foam (Goodfellow, 99.5 %) of 0.5 × 1.5 cm^2 was cleaned in isopropanol, HCl 3.0 mol L^{-1} solution, and distilled water under ultrasonication for 10 min each. Finally, the Ni foam substrates were treated under N_2 plasma (Zhengzhou CY-P2L-B) with 80 W of radiofrequency for 60 s. The deposition bath was prepared with the fixed P concentration of 0.25 mol L^{-1} and the different concentrations of Ni (6.25; 12.5; 25; 37.5 mMol L^{-1}). The Ni-P coatings prepared with the different Ni:P concentrations were nominated 1-Ni-P /NF, 2-Ni-P /NF, 3-Ni-P /NF, and 4-Ni-P /NF for the 6.25; 12.5; 25; 37.5 mMol L^{-1}. The precursors of metal phosphide deposition were $NiCl_2{\cdot}6H_2O$, $NaH_2PO_2{\cdot}H_2O$, and 0.2 mol L^{-1} NH_4Cl as supporting electrolytes. The pH of the deposition bath was maintained at pH 4. All films were obtained from potentiodynamic deposition at –250 mA for 15 min under stirring at room temperature. After electrodeposition, the films were dried under a vacuum at 70 °C overnight.

2.2. Characterization

Scanning electron microscope images were obtained using an FEI microscope model Inspect F5, to analyze the film morphologies. Atomic compositions were obtained from an energy-dispersive spectroscopy (EDS) unit, model Thermo Scientific Ultra Dry attached to a FEG (JEOL-JSM-7500F) microscope operating at 10 eV. X-ray diffraction spectra were performed using a Shimadzu instrument (XRD-6000) with Cu Kα radiation (1.5406 Å, 40 kV). X-ray photoelectron spectroscopy was analyzed using a Scienta Omicron spectrometer, ESCA 2SR model with radiation source Al Kα (1486.7). The elemental quantitation and deconvolution of the Ni and P elements were performed using the Casa XPS software (version 2.3). The high resolution transmission electron microscope (HR-TEM) images were acquired using a Jem-2100 Jeon under an accelerating voltage of 200 kV coupled with an INCA energy TEM 200.

2.3. Electrochemical analysis

A potentiostat/galvanostat Autolab model PGSTAT302N was used for all electrochemical tests using a three-electrode configuration cell. For these measurements, an Ag/AgCl electrode was used in acidic and neutral solutions (0.5 mol L^{-1} H_2SO_4 and 1 mol L^{-1} PBS, respectively), and a Hg/HgO electrode for alkaline solution (1.0 mol L^{-1} KOH) was used as reference electrodes, and as the counter electrode a graphite rod. The metal phosphide-modified Ni foam working electrodes were used with an exposed area of 1 cm^2. All the solutions were used at 25 °C. The potential reference values were converted:

$$Acidic\ and\ Neutral:\ E\ (vs.\ RHE) = E(Ag/AgCl_{(KClsat.)}) + 0.197 + 0.059 \times pH$$

$$Alkaline:\ E\ (vs.\ RHE) = E(Hg/HgO) + 0.098 + 0.059 \times pH$$

The linear sweep voltammetry (LSV) curves were performed at 1 mV s^{-1} scan rate without *iR* compensation. The Pt/C electrode used for electroactivity comparison was prepared by drop-casting an ink of dispersed commercial Pt/C (20 mg, 20 wt.% Pt on graphitized carbon, Sigma-Aldrich) in ethanol (1 mL) and Nafion® 117 solution (160 μL, 5 wt.%, Sigma-Aldrich). The electrode was prepared by depositing 200 μL of the Pt/C ink onto Ni foam (1 × 2 cm^2) and dried at 40 °C. Before registering polarization curves, the prepared Ni-P electrodes were polarized at –50 mA cm^{-2} for 15 min. EIS analysis was performed at −50 mV_{RHE} and OCP with 10 mV amplitude in the frequency range of 10 kHz to 10 MHz in alkaline electrolyte. Chronopotentiometry tests were conducted by applying –100 mA cm^{-2} in acidic and alkaline solutions for at least 16 h. The Electrochemical Active Surface Area (ESCA) was determined by double-layer capacitance (C_{dl}) measurements in unequal scan rates of 50, 75, 100, 125, and 150 mV s^{-1} (see Supplementary Material). Faradaic efficiency was determined using an H-type cell assembled with the 3-Ni-P / P electrode as a cathode coupled with a gas drainage system. The H-cell was separated using an N117 Nafion membrane, and the electrolysis was performed at a constant applied current density of −100 mA cm^{-2} for 1.5 h.

3. Results and discussion

The nickel phosphide films were prepared *in situ* and grown on the 3D metallic nickel foam substrate galvanostatically (Fig. 1) at −0.25 A. The Ni-P film deposition occurs by simultaneous Ni^{+2} and $H_2PO_2^-$ reduction. The XRD patterns of the as-obtained NiP films on the NF (Fig. S1) show no measurable extra crystalline peaks compared with the unmodified substrate, only a feeble swell in the catalysts diffraction patterns suggesting a weak crystallinity of all the electrodeposited metal phosphide coating.

Scanning electron microscopy was performed to characterize the Ni-P coatings in the 3D substrate. SEM images for the 3-Ni-P coated 3D substrate are presented in Fig. 2a and b. The SEM images showed that the electrodeposition method provided a granular Ni-P film within the 3D NF integrated framework structure. The SEM images of the Ni-P with different Ni molar ratios are presented in Fig. S2 (Supplementary Material). The concentration of the Ni precursor influences the effectiveness of the metallic support coating. The lowest Ni molar ratio presents lower coverage of the NF, and the coating becomes more uniform as the concentration increases. In addition, the 1-Ni-P and 2-Ni-P films present globular morphology, while the 4-Ni-P electrode presents cracked clay morphology. The 3-Ni-P film surface is composed of microspheres with some cracked clay structure. The cracks on the surface of electrodeposited films have already been observed in the literature [18–20] and are attributed to the mutual extrusion of the metal phosphide microspheres [21]. The elemental composition of the 3-Ni-P/NF electrode was confirmed by dispersive spectroscopy, which is Ni, P, and O elements (Fig. S3) with atomic content of 71.0 %, 19.0 %, and 10 %, respectively (Table S1). The Ni-P film co-deposition mechanism induced by the electrodeposition method enables the incorporation of 12–15 % P [22,23] at high current densities.

The structure and morphology of the 3-Ni-P catalyst were analyzed by transmission electron microscopy. TEM images for the 3-NiP/NF sample presented in Fig. 2c and d shows the granular structure of the nickel phosphide catalyst. High-resolution transmission microscopy (HRTEM) demonstrates the highly amorphous structure of the nickel phosphide catalyst along with a few weak crystalline regions. In Fig. 2e, the lattice fringes with interplanar spacing of $d = 0.22$ and $d = 0.24$ nm correspond to the Ni_2P (111)[24,25] and NiP_2 (210)[26] crystal phases. Despite these regions of low crystallinity, it appears that the material has a predominantly amorphous structure, in agreement with the results of

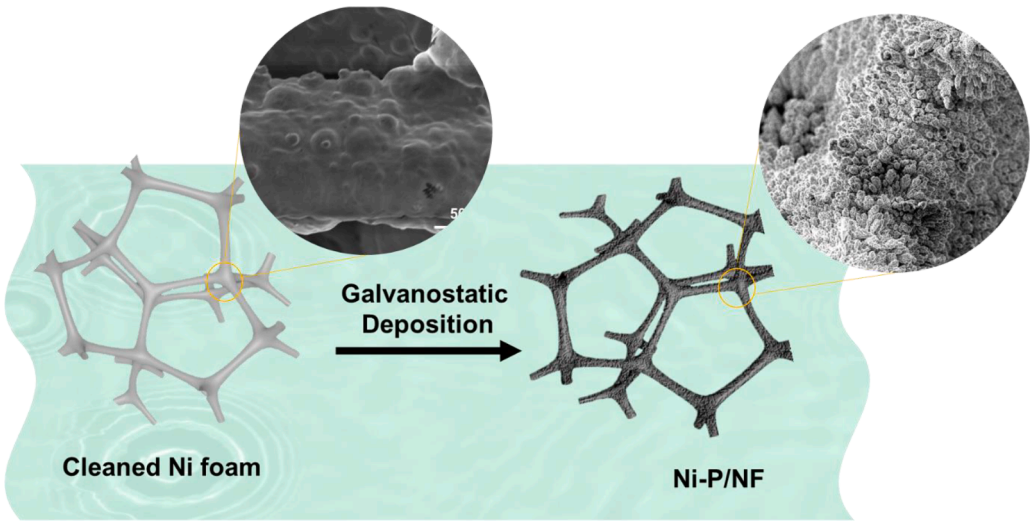

Fig. 1. Schematic illustration of the Ni-P/NF electrode synthesis.

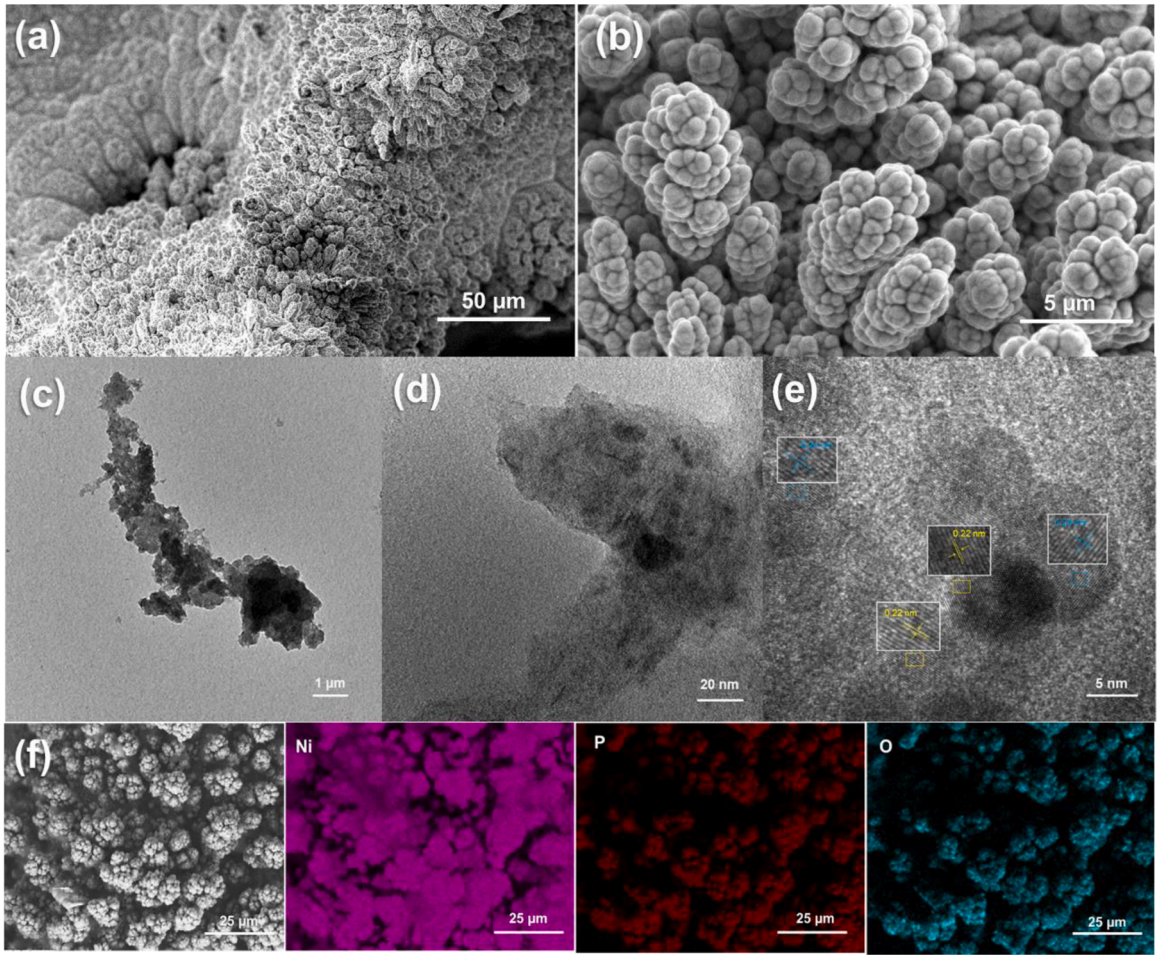

Fig. 2. (a-b) Scanning electron micrographs of the 3-Ni-P catalyst film on the Ni foam substrate with different magnifications. (c-d) TEM and (e) HRTEM images of the 3-Ni-P/NF; (f) EDS-SEM mapping images for the 3Ni-P electrode.

the XRD analysis. As verified in contact angles analysis (Fig. S4), the deposition of the amorphous 3-Ni-P film on the NF substrate resulted in a more hydrophilic surface that can lead to better H_2 gas bubble detachment during the HER. The EDS-SEM elemental mapping (Fig. 2f) shows that nickel and phosphorus are uniformly distributed over the 3-Ni-P film.

XPS analysis revealed the valence states of the elements and surface chemical compositions of the 3-Ni-P deposited film. The survey spectra in Fig. 3a of the electrode surface suggest that Ni, O, C, and P are present. The calibration of the binding energies was made using the C 1 s equal to

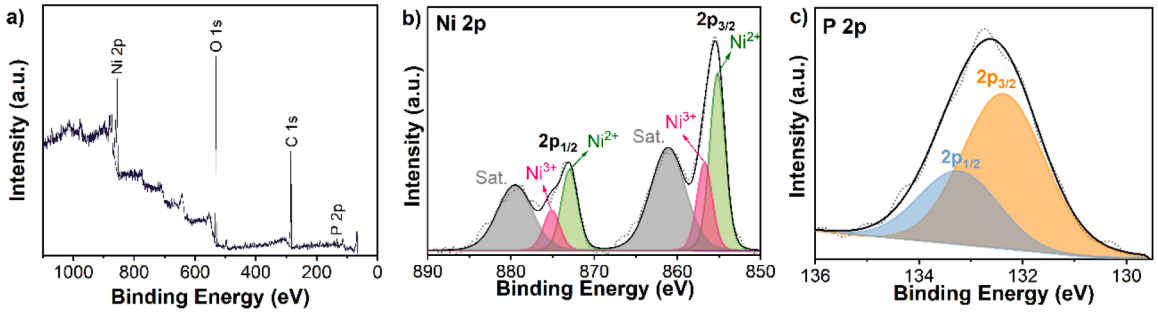

Fig. 3. XPS spectra of the 3-Ni-P/NF electrode: (a) the survey spectrum, (b) Ni 2p, and (c) P 2p.

284.5 eV [27]. The high-resolution Ni 2p region is shown in Fig. 3b with Ni $2p_{3/2}$ and $2p_{1/2}$ regions, along with two satellites at 861.16 and 879.51 eV, respectively [28,29]. The deconvoluted peaks corresponding to the $Ni^{2+}$and Ni^{3+} ions are at 856.81 and 875.11 eV, respectively [29, 30]. The absence of any peaks related to metallic nickel (Ni^0) is indicative that the substrate surface was fully covered by the NiP catalyst film [31], as verified by the SEM analysis. Fig. 3c presents the high-resolution spectrum of P 2p, and the deconvoluted peaks at 132.41 and 133.26 eV correspond to $2p_{3/2}$ and $2p_{1/2}$, respectively, which is assigned to the P-O bond in the PO_4^{3-} a species that appears due to the superficial oxidation of the deposited film [32,33].

3.1. *Electrocatalytic HER performances*

The HER electrocatalytic activity of the amorphous nickel-phosphide electrodes was investigated in alkaline media (1.0 mol L^{-1} KOH). The HER performance for the bare substrate and Pt/C/NF were examined for comparison. Fig. 4a shows all the LSV curves with IR-drop compensation (the R_s values corresponding to each polarization curve were obtained from EIS). The LSV curve for the 3-Ni-P/NF electrode without IR compensation is presented in Fig. S5. The best-performing film would be the one that presented lower overpotentials at –10 and –100 mA cm^{-2}. According to Fig. 4a, the 3Ni-P requires an overpotential to reach –10 mA cm^{-2} of 69 mV, which is significantly lower than those for 1–Ni-P (125 mV), 2Ni-P (91 mV), 4-Ni-P (98 mV) and bare NF substrate (250 mV). Although higher than the commercial Pt/C electrode overpotential (36 mV). Fig. 4b displays the overpotentials η_{10} and η_{100} for all the prepared samples. The 3-Ni-P electrode possesses superior performance even for large current densities. Remarkably, the Ni-P electrode performed better for >250 mA cm^{-2} than the Pt/C (20 %) electrode. Such intrinsically superior HER activity should be attributed to the granular Ni-P structure supported in the NF 3D network, which results in good

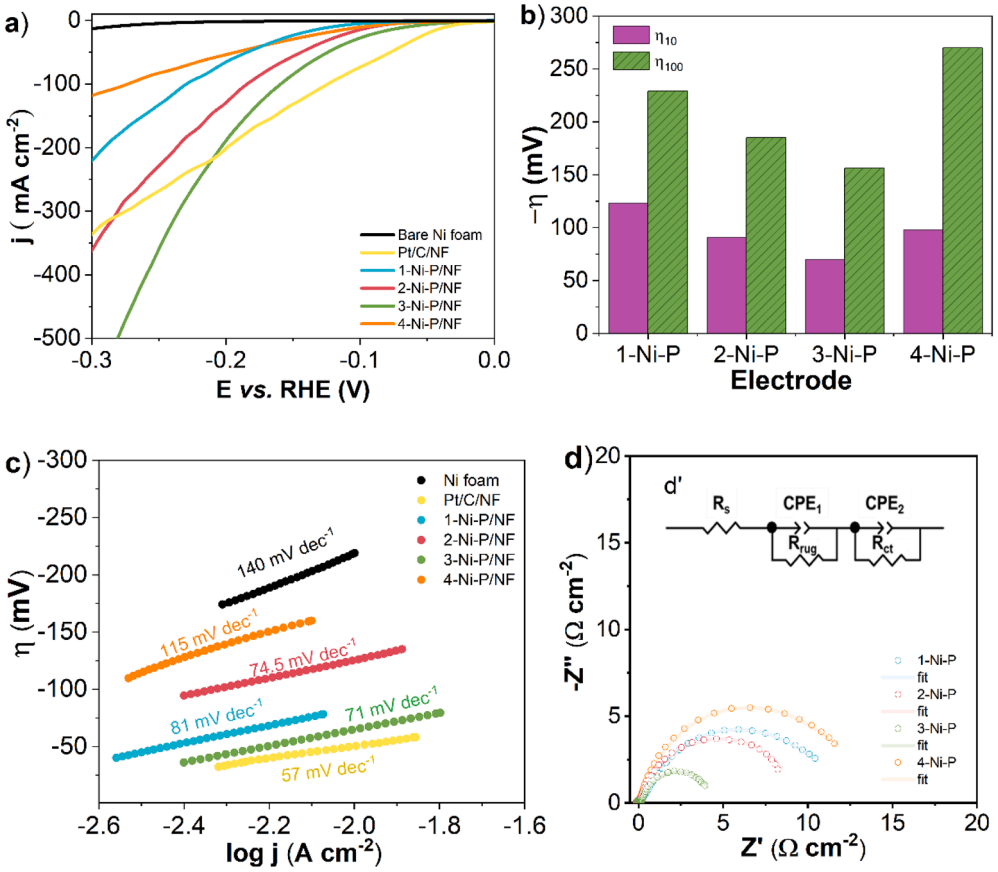

Fig. 4. (a) HER Polarization curves registered in 1.0 mol L^{-1} KOH at 1 mV s^{-1}, (b) Comparison of the η_{10} and η_{100} values, (c) Tafel plots of NF, Pt/C NF, and Ni-P/NF electrodes prepared with the different Ni ratios. (d) Nyquist plots at −50 mV_{RHE} for the Ni-P/NF electrodes. Insert: d' Equivalent circuit EIS.

conductivity and hydrophilicity favoring H_2 bubbles release, especially at high current densities [34].

As a way to investigate the HER kinetics of the Ni-P electrodes, Tafel slopes were derived from fitting the linear portion of the replotted LSV curves. As seen in Fig. 4c, the 3Ni-P electrode possesses a slight Tafel slope of 71 mV dec^{-1} compared to the other electrodeposited Ni-P electrodes, significantly smaller than the bare NF electrode (140 mV dec^{-1}). The Tafel slope values (Table 1) indicate that the Ni-P electrode follows the Volmer-Heyrovsky mechanism [35,36]. The Volmer-Heyrovsky mechanism starts with the water molecule adsorption followed by cleavage of the O—H bond by electron transferring from the electrode surface to form H_{ads}* species. The H_2 molecule is produced from the reaction between the adsorbed hydrogen atoms and water molecules from alkaline [35]. The Tafel slope value decrease with the 3Ni-P electrode indicates that the water dissociation step has been significantly accelerated compared to the Ni foam and the Ni-P electrodes, implying higher catalytic activity. The calculated values demonstrate a tendency to lower the Tafel coefficients with the increase of the Ni ratio in the deposition. The positively charged nickel anions will likely form nickel oxyhydroxide at the electrode/electrolyte interface by adsorbing the hydroxide ions (OH^-)[37,38]. Previous reports have observed the formation of interfacial oxide-hydroxides for self-supported metal phosphide electrodes. These interfacial hydroxide sites strongly promote the water dissociation step (Volmer step), enhancing the kinetics for the HER [39] process, which results in the lowest Tafel coefficient values. As observed previously, the 4Ni-P/ NF cannot perform as well as the other prepared electrodes, presenting the highest Tafel slope closer to NF. The poor performance suggests that the excessive $Ni(OH)_2$ [40] at the electrode surface hinders the performance of the Ni-P phase, which is superior to the $Ni(OH)_2$ electrodes reported in the literature. The exchange current density (j_0), related to the catalyst activity at potential $\eta=0$, is also obtained from the Tafel plots. The calculated j_0 values for the electrodeposited Ni-P electrodes are presented in Table 1. Notably, the j_0 of the 3Ni-P/NF is 2.289 mA cm^{-2}, slightly lower than the Pt/C electrode (2.59 mA cm^{-2}). The elevated j_0 obtained with the optimized Ni-P electrode reflects in the enhancement of the electrocatalyst electron transfer rate for the reaction [41], which justifies the superior HER performance compared to the literature (Table S7).

EIS measurements were carried out to compare the kinetics of the Ni-P samples. Fig. 4d shows the Nyquist plots of the Ni-P / NF electrodes performed at −50 mV_{RHE}. The Nyquist diagrams were fitted using the equivalent circuit in Fig. 4d' to estimate the charge transfer resistance values (Table S2). As displayed in Table S2, the 3-Ni-P/NF electrode presented had a significantly smaller charge transfer resistance (4.22 Ω cm^{-2}) than 1-Ni-P (11.30 Ω cm^{-2}), 2-Ni-P (9.34 Ω cm^{-2}) and 4-Ni-P (12.79 Ω cm^{-2}), demonstrating enhanced charge transfer that leads to superior HER. The 3-Ni-P electrode has a much lower charge transfer resistance than the 4-Ni-P electrode. These results endorse the generation of excessive $Ni(OH)_2$ at the 4-Ni-P electrode surface since the electrical conductivity of the electrode is significantly diminished [42, 43].

We estimated the electrochemically active surface area (ECSA) of the Ni-P catalytic films to gain further insights into the Ni-P electrode's intrinsic activity. The cyclic voltammograms (Fig. 5a) registered from 50 to 150 mVs^{-1} data displayed in Fig. S6 were used to estimate the double-layer capacitance (C_{dl}). As presented in Fig. 5b, the 3-Ni-P electrode exhibits a high C_{dl} value of 10.03 mF cm^{-2}, remarkably larger than 1-Ni-P (3.53 mF cm^{-2}), 2-Ni-P (4.95 mF cm^{-2}) and 4Ni-P (4.04 mF cm^{-2}). This value is superior to other Ni-rich phosphides reported in the literature [44,45] 8.64 mF cm^{-2} and 5.82 mF cm^{-2}. A higher C_{dl} value observed for the 3-Ni-P electrode may be associated with more exposure to the active sites and indicate that the optimum nickel content in the deposition bath is used to synthesize the film. This results in a structured microsphere film that facilitates active site access. From the C_{dl} values, we estimated the electrochemical active surface area (ECSA), and the roughness factor (RF) was estimated by the ratio of the electrode geometric area [46] for the Ni-P films deposited with the different baths (Table S3). The ECSA (Fig. 5c) increases gradually with the nickel precursor concentration, achieving a maximum in the 3-Ni-P electrode. This increase at ECSA and RF suggests the deposition of a more uniform and porous coating at the NF substrate that can often provide more exposed active sites, sufficient mass transport, and superior HER performance.

In contrast, there is a decrease in the ECSA and RF values for the electrode prepared with the highest Ni concentration (4-Ni-P), resulting from the aggregation of the electrodeposited particles that leads to a more compact shrinkage morphology of the film hindering the exposure of the active sites and even affects the interaction with the electrolyte [47]. The normalization of the LSV curves by the ECSA was performed to exclude the surface area effect and compare the intrinsic activity of the Ni-P electrodes for HER (Fig. 5d). Even after the normalization, the 3-Ni-P electrode performs best among all the prepared electrodes. The Ni-P films' Turnover Frequency (TOF) was estimated from the ECSA results to understand its intrinsic properties. As shown in Table S3, the 3-Ni-P electrode presents the highest TOF value of 0.64 s^{-1} at –100 mV, justifying its superior HER performance compared with the other prepared electrodes. In this sense, the excellent electrocatalytic activity of the 3-Ni-P electrode for alkaline HER is attributed to the large ECSA and low electron transfer resistance.

Long-term stability is a critical requirement for an efficient electrocatalyst. Therefore, the 3Ni-P electrode stability was investigated by constant current density chronopotentiometry at −100 mA cm^{-2} in 1.0 mol L^{-1} KOH solution. The Ni-P electrode presented negligible degradation during the long-term electrolysis, as shown in Fig. 6a. As fresh electrolyte was added, the electrode returned to the initial overpotential and remained stable. Moreover, the LSV curves showed insignificant differences before and after polarization (previous and after adding fresh electrolyte (see Fig. 6b). After the 30 h electrolysis, the 3-Ni-P sample was characterized using SEM. Fig. 6c and d show a morphological change in the shape of microspheres to a more compact structure. This slightest change in the film morphology seems to result from a structural reorganization but did not influence the nickel phosphide electrode stability of the material. The EDS patterns (Fig. S7) show a significant increase in the oxygen content in the Ni-P sample. Contact-angle analysis of the 3-Ni-P (Fig. S8) demonstrated the enhancement at the surface hydrophilicity continuous electrolysis. This phenomenon is associated with surface restructuration. The XPS analysis after long-term electrolysis (Fig. S12) reveals a relative decrease in the Ni^{2+}region (Fig. S12e) in comparison with the freshly prepared electrode (Fig. 2). In addition, it was possible to verify a doublet related to the nickel specie in metallic form (Ni^0). An interesting result in the P 2p high-resolution spectra (Fig. S12f) was verified, showing deconvoluted peaks at 129.8 and 130.3 eV assigned to the P-Ni bond, indicating the removal of surface oxides during the electrolysis test. The outstanding stability of the 3-Ni-P electrode can be attributed to its relatively high roughness factor and surface hydrophilicity, enabling a good interaction with the electrolyte and facilitating the bubble release.

The H_2 production generated during the HER in alkaline media was determined by a drainage method coupled with gas-chromatography analysis. The H_2 volume was collected during the 90-minute electrolysis at –100 mA cm^{-2}. As observed in Fig. 7a, the 3NiP/NF electrode

Table 1
Parameters of HER for the Ni-P electrodes in KOH 1.0 mol L^{-1}: overpotentials and Tafel parameters.

Electrode	η_{10} (mA cm^{-2})	η_{100} (mA cm^{-2})	b (mV dec^{-1})	j_0 (μA cm^{-2})
1-Ni-P/NF	123	229	81.0	260
2-Ni-P/NF	91	185	74.5	490
3-Ni-P/NF	69	156	71	2289
4-Ni-P/NF	98	270	115	675

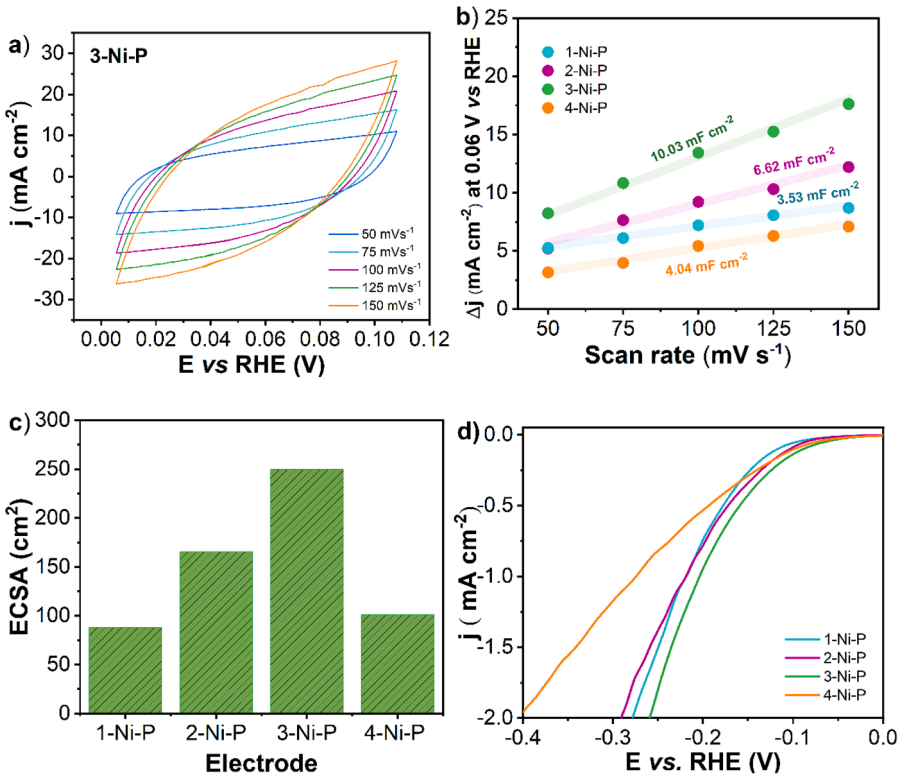

Fig. 5. (a) Cyclic voltammetry at 50, 75, 100, 125, and 150 mV s^{-1} in the capacitive potential range of the 3Ni-P/ NF. (b) Capacitive currents at −0.06 V *vs.* RHE for the Ni-P electrodes at different scan ranges. (c) Estimated ECSA values and (d) Electrochemical surface area-normalized polarization curves of the deposited Ni-P electrodes.

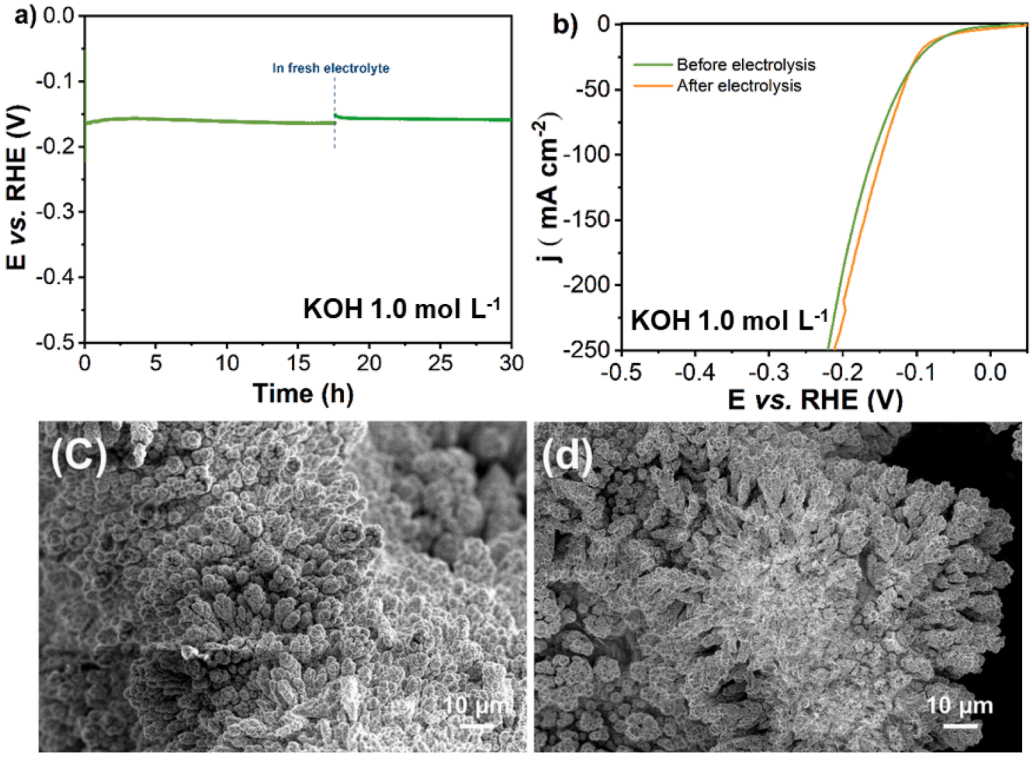

Fig. 6. (a) Constant-current stability of the 3Ni-P/ NF electrode at –100 mA cm^{-2} for 30 h. (b) The polarization curves registered before and after the steady-state electrolysis. SEM micrographs of the 3Ni-P electrode before (c) and after (d) electrolysis.

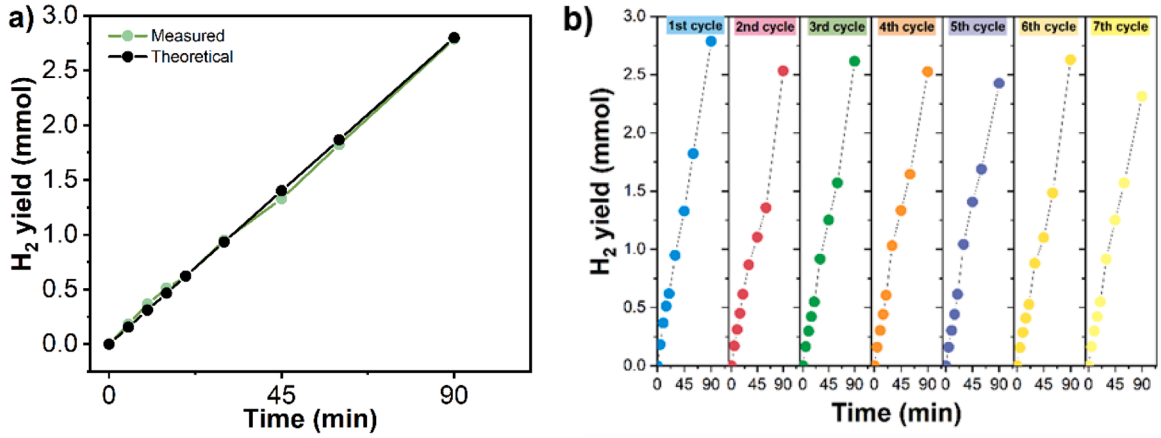

Fig. 7. (a) Experimentally measured and theoretically calculated H_2 production by overall water splitting in 1.0 mol L^{-1} KOH (at ~ −100 mA cm^{-2} during 90 min), (b) H_2 production stability test in 7 cycles of 3Ni-P/NF at –100 mA cm^{-2} for 90 min.

exhibited high efficiency for H_2 production, consistent with the theoretical values. Furthermore, the electrode showed performance stability during the high-current alkaline electrolysis during 7 cycles of 90 min each. Fig. 7b shows that the nickel phosphide electrode catalytic activity was maintained even after its application at a high current for the 7-cycle test, presenting only small fluctuations mainly due to leakage losses. The results confirm the excellent performance of the electrodeposited nickel phosphide electrode towards the HER in alkaline media with high efficiency and stability.

Considering an ideal electrocatalyst should operate efficiently in various pH, the 3-Ni-P/NF optimized electrode was evaluated for HER in acidic (0.5 mol L^{-1} H_2SO_4) and neutral electrolyte (1.0 mol L^{-1} PBS). As for the alkaline medium experiments, all the potentials were corrected with iR compensation. Fig. 8a presents the polarization curves registered for the freshly prepared Ni-P electrodes in the different pH electrolytes. In acidic media, the 3-Ni-P electrode delivers 45 and 122 mV to drive the current densities –10 and –100 mA cm^{-2}, respectively. Fig. 8b shows that the 3-Ni-P electrode presents lower electrocatalytic activity in 1 mol L^{-1} PBS than for extreme pH conditions. Although the overpotentials in neutral are higher than for the acidic and alkaline conditions, the electrode presented competitive and comparable performance to other electrodes reported in the literature (Table S9). The kinetics for HER was evaluated for the different pH range by constructing Tafel plots (Fig. 8c). The 3-Ni-P electrode presented Tafel slopes of 49, 71, and 139.3 mV dec^{-1} for acidic, alkaline, and neutral environments, respectively, indicating that for pH universal, the 3-Ni-P electrode obeys the Volmer-Heyrovsky mechanism. Under neutral conditions, the high Tafel slope and overpotential values reflect the slow kinetics. This slow kinetics is due to the HER mechanism's complexity since water molecules and dissociated H_3O^+ ions participate in the H_2 production mechanism [48, 49].

Moreover, the higher electrolyte resistance of neutral electrolytes requires extra energy input to drive the reaction. The electrochemical HER is pH-dependent since it reflects in the reactant species and the whole local electrochemical environment surrounding the catalyst's active sites. On the other hand, the performance in acidic and alkaline

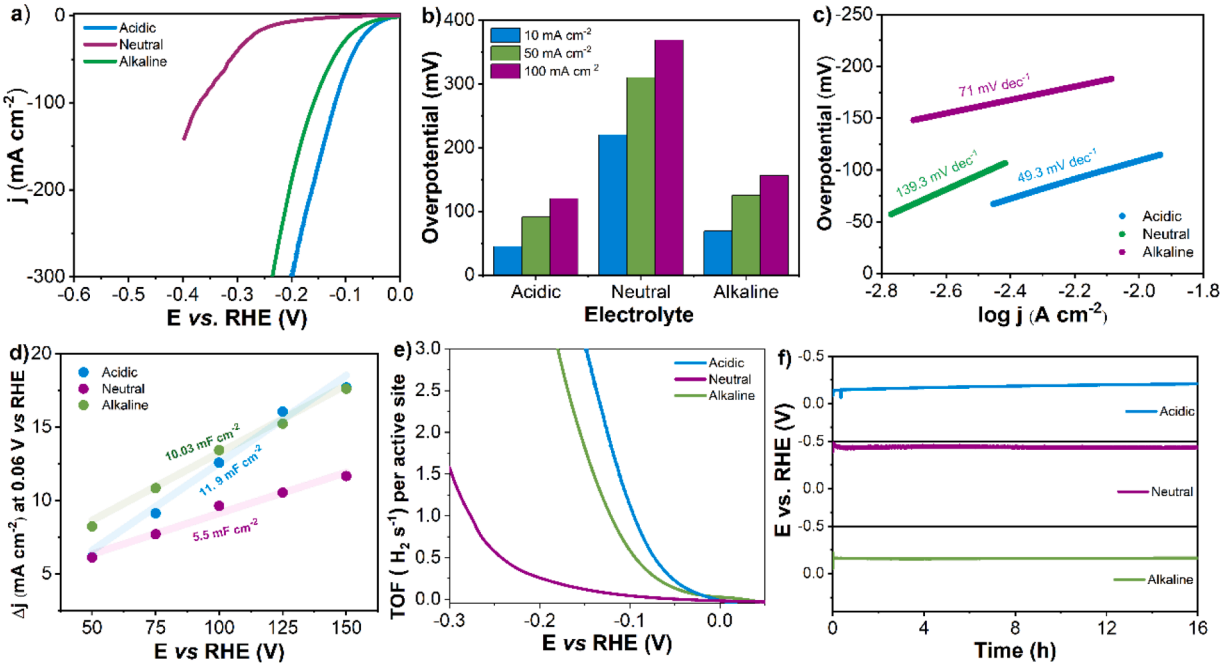

Fig. 8. HER activities of 3-Ni-P / NF in 0.5 mol L^{-1} H_2SO_4, 1 mol L^{-1} PBS, and 1 mol L^{-1} KOH, (a) Polarization curves, (b) Overpotential values η_{10}, η_{50}, and η_{100}, (c) Tafel plots for the 3Ni-P/NF electrode, (d) Comparison of the C_{dl} at different pH, (e) TOF curves and (f) Stability test for the 3Ni-P / NF at –100 mA cm^{-2} for 16 h.

conditions presented extremely low overpotentials for both –10, –50, and –100 mA cm^{-2} and small Tafel slope values, demonstrating excellent reaction kinetics. The ECSA was also estimated for the 3-Ni-P at the electrolytes. The C_{dl} values obtained for the 3-Ni-P (Fig. 8d) show extreme pH electrolytes are similar to 10.03 mF cm^{-2} for alkaline and 11.9 mF cm^{-2} for acidic. The ECSA estimated from the C_{dl} values were also similar (Table S5), demonstrating that the electrodeposited electrode presents large ECSA in both pHs that contribute to the excellent performance of these electrodes.

Moreover, a normalization of LSV curves was made to exclude the contribution of the ECSA (Fig. S9). It is observed that the intrinsic activity observed for the 3-Ni-P electrode in alkaline and acidic media is similar. As for the neutral condition performance, lower catalytic activity is observed, probably due to the electrolyte's lower conductivity and lower kinetics towards HER. The higher intrinsic activity for alkaline and acidic media is presented in the TOF curves in Fig. 8e. The 3-Ni-P electrode presented TOF values of 1.14 s^{-1}, 0.59 $s^{-1,}$ and 0.05 s^{-1} for acidic, alkaline, and neutral conditions. The high TOF values are attributed to the high density of surface exposed active sites that provide excellent performance towards HER. These values are higher than the reported for metal phosphide-based catalysts (see Table S6).

The electrode stability for the broad pH range was evaluated by continuous electrolysis at –100 mA cm^{-2} (Fig. 8f). For the test in acidic media, an overpotential fluctuation arises after 12 h of operation. Such a phenomenon was not observed for alkaline and neutral electrolysis (Fig. 8f). The 3-Ni-P/NF film surfaces were characterized by SEM and XPS analysis after the continuous electrolysis. From the post-electrolysis SEM images presented in Fig. S11, it is verified that for the electrode tested in the acidic electrolyte, the exposure of the Ni foam substrate indicates material loss during the electrolysis. This assumption is reinforced by the XPS analysis after long-term electrolysis (Fig. S12), in which no peaks assigned to P species was verified (Fig. S12b). For the post-electrolysis test in neutral conditions, the electrode morphology remained composed by microspheres, but it was also possible to verify a certain loss of material. This slightest change in the film morphology seems to result from a structural reorganization but did not influence the nickel phosphide electrode stability of the material. The XPS analysis after long-term electrolysis test is shown in Fig. S12. The film maintenance was verified not only by the Ni 2p high-resolution spectra (Fig. S12c), showing the deconvoluted peaks corresponding to Ni^{2+} and Ni^{3+} ions, but also with the preservation of P-Ni bond in the high-resolution spectra of S 2p (Fig. S12d). Tables S7–S9 shows that the electrodeposited 3-Ni-P film presented superior electrocatalytic performance to almost all previously reported electrodeposited metal-phosphide electrocatalysts in literature. Furthermore, the 3-Ni-P electrode performance was comparable to the catalysts prepared with multiple steps and high-temperature thermal treatment. Therefore, the electrodeposited 3-Ni-P electrode presented excellent features for application in HER at a wide pH range.

4. Conclusions

In summary, a highly efficient Ni-P/NF electrode was successfully synthesized through one-step electrodeposition at high current density. The Ni content in the deposition bath affected the Ni-P electrode performance. An optimum Ni concentration leads to superior performance at low overpotentials in a wide pH range. The distinct performance of the 3-Ni-P/ NF electrode is attributed to its large surface area and roughness, enabling better interaction with the electrolyte. Remarkably, the 3-Ni-P can efficiently drive the HER with overpotentials in a wide pH range with long durability. Furthermore, the 3-Ni-P electrode deposited in a single step showed electrocatalytic activity superior in pH-universal compared to different metal Ni-phosphide-based catalysts previously described, which were synthesized via several steps and thermal treatment. Thus, this work demonstrates that the electrodeposition method is excellent for developing facile-scalable and highly stable NiP electrocatalysts for the hydrogen evolution reaction in pH-universal conditions.

CRediT authorship contribution statement

A.B. Silva: Conceptualization, Investigation, Writing – original draft. **M. Medina:** Writing – review & editing, Data curation. **L.A. Goulart:** Writing – review & editing. **L.H. Mascaro:** Supervision, Project administration, Writing – review & editing.

Declaration of Competing Interest

The authors declare that they have no known competing financial interests or personal relationships that could have appeared to influence the work reported in this paper.

Data availability

No data was used for the research described in the article.

Acknowledgments

Fundação de Amparo a Pesquisa do Estado de São Paulo, FAPESP, by funding the research, grant number #2020/11756-2 #2017/11986-5, #2017/12794-2 and #2013/07296-2. Conselho Nacional de Desenvolvimento Científico e Tecnológico, CNPq, grant number #152607/2022-6, #311769/2022-5 and #406156/2022-0, FINEP-Financiadora de Estudos e Projetos grant number #01.22.0179.00. The authors also thank Shell and the strategic importance of the support given by ANP (Brazil's National Oil, Natural Gas, and Biofuels Agency) through the R&D levy regulation.

Supplementary materials

Supplementary material associated with this article can be found, in the online version, at doi:10.1016/j.electacta.2023.143679.

References

[1] IEA, Global Hydrogen Review 2021, 2021.
[2] J. Rosenow, N. Eyre, Reinventing energy efficiency for net zero, Energy Res. Soc. Sci. 90 (2022), https://doi.org/10.1016/j.erss.2022.102602.
[3] J. Cooper, L. Dubey, S. Bakkaloglu, A. Hawkes, Hydrogen emissions from the hydrogen value chain-emissions profile and impact to global warming, Sci. Total Environ. 830 (2022), 154624, https://doi.org/10.1016/j.scitotenv.2022.154624.
[4] X. Zou, Y. Zhang, Noble metal-free hydrogen evolution catalysts for water splitting, Chem. Soc. Rev. 44 (2015) 5148–5180, https://doi.org/10.1039/C4CS00448E.
[5] H. Xu, J. Wan, H. Zhang, L. Fang, L. Liu, Z. Huang, J. Li, X. Gu, Y. Wang, A new platinum-like efficient electrocatalyst for hydrogen evolution reaction at all pH: single-crystal metallic interweaved V8C7 networks, Adv. Energy Mater. 8 (2018), https://doi.org/10.1002/aenm.201800575.
[6] R.B. Wexler, J.M.P. Martirez, A.M. Rappe, Active role of phosphorus in the hydrogen evolving activity of nickel phosphide (0001) surfaces, ACS Catal. 7 (2017) 7718–7725, https://doi.org/10.1021/acscatal.7b02761.
[7] C. Li, H. Gao, W. Wan, T. Mueller, Mechanisms for hydrogen evolution on transition metal phosphide catalysts and a comparison to Pt(111), Phys. Chem. Chem. Phys. 21 (2019) 24489–24498, https://doi.org/10.1039/C9CP05094A.
[8] C. Hu, J. Cai, S. Liu, C. Lv, J. Luo, M. Duan, C. Chen, Y. Shi, J. Song, Z. Zhang, A. Watanabe, E. Aoyagi, S. Ito, General strategy for preparation of porous nickel phosphide nanosheets on arbitrary substrates toward efficient hydrogen generation, ACS Appl. Energy Mater. 3 (2020) 1036–1045, https://doi.org/10.1021/acsaem.9b02067.
[9] Y. Wang, L. Liu, X. Zhang, F. Yan, C. Zhu, Y. Chen, Self-supported tripod-like nickel phosphide nanowire arrays for hydrogen evolution, J. Mater. Chem. A Mater. 7 (2019) 22412–22419, https://doi.org/10.1039/c9ta07859b.
[10] A. Chen, L. Fu, W. Xiang, W. Wei, D. Liu, C. Liu, Facile synthesis of Ni5P4 nanosheets/nanoparticles for highly active and durable hydrogen evolution, Int. J. Hydrogen Energy 46 (2021) 11701–11710, https://doi.org/10.1016/j.ijhydene.2021.01.079.
[11] H.-M. Zhang, J.-J. Wang, Y. Meng, J. Sun, Recent advances in amorphous metal phosphide electrocatalysts for hydrogen evolution reaction, Int. J. Hydrogen Energy (2022), https://doi.org/10.1016/j.ijhydene.2022.08.184.

[12] A.R.J. Kucernak, V.N. Naranammalpuram Sundaram, Nickel phosphide: the effect of phosphorus content on hydrogen evolution activity and corrosion resistance in acidic medium, J. Mater. Chem. A Mater. 2 (2014) 17435–17445, https://doi.org/10.1039/c4ta03468f.

[13] A.B. Laursen, R.B. Wexler, M.J. Whitaker, E.J. Izett, K.U.D. Calvinho, S. Hwang, R. Rucker, H. Wang, J. Li, E. Garfunkel, M. Greenblatt, A.M. Rappe, G.C. Dismukes, J.I. Murray, A. Bauer, N.D. Fessner, D.L. Dunklemann, O. Bob-egbe, H.S. Rzepa, J. Richardson, A.C. Spivey, Supporting information, ACS Catal. 8 (2018) 4408–4419.

[14] D. Zhang, J.Z. Soo, H.H. Tan, C. Jagadish, K. Catchpole, S.K. Karuturi, Earth-abundant amorphous electrocatalysts for electrochemical hydrogen production: a review, Adv. Energy Sustainab. Res. 2 (2021), 2000071, https://doi.org/10.1002/aesr.202000071.

[15] G. Liu, F. Hou, X. Wang, B. Fang, Stainless steel-supported amorphous nickel phosphide/nickel as an electrocatalyst for hydrogen evolution reaction, Nanomaterials (2022) 12, https://doi.org/10.3390/nano12193328.

[16] F. Bao, E. Kemppainen, I. Dorbandt, R. Bors, F. Xi, R. Schlatmann, R. van de Krol, S. Calnan, Understanding the hydrogen evolution reaction kinetics of electrodeposited nickel-molybdenum in acidic, near-neutral, and alkaline conditions, ChemElectroChem 8 (2021) 195–208, https://doi.org/10.1002/celc.202001436.

[17] S. Jo, B. Kang, H. Oh, J. Kwon, P. Choi, K.-Y. Cho, J.-H. Lee, K. Eom, Reconstruction of a surficial P-rich layer on Ni-P electrocatalysts for efficient hydrogen evolution applicable in acidic and alkaline media, Chem. Eng. J. 457 (2023), 141138, https://doi.org/10.1016/j.cej.2022.141138.

[18] X. Xu, T. Guo, J. Xia, B. Zhao, G. Su, H. Wang, M. Huang, A. Toghan, Modulation of the crystalline/amorphous interface engineering on Ni-P-O-based catalysts for boosting urea electrolysis at large current densities, Chem. Eng. J. 425 (2021), https://doi.org/10.1016/j.cej.2021.130514.

[19] D. Guo, D. Duan, J. Gao, X. Zhou, S. Liu, Y. Wang, Synthesis of nest-like porous MnCo–P electrocatalyst by electrodeposition on nickel foam for hydrogen evolution reaction, Int. J. Hydrogen Energy 47 (2022) 6620–6630, https://doi.org/10.1016/j.ijhydene.2021.12.011.

[20] W. Li, M. Chen, Y. Lu, P. Qi, G. Liu, Y. Zhao, H. Wu, Y. Tang, One-pot electrodeposition synthesis of NiFe-phosphate/phosphide hybrid nanosheet arrays for efficient water splitting, Appl. Surf. Sci. 598 (2022), https://doi.org/10.1016/j.apsusc.2022.153717.

[21] D. Duan, D. Guo, J. Gao, S. Liu, Y. Wang, Electrodeposition of cobalt-iron bimetal phosphide on Ni foam as a bifunctional electrocatalyst for efficient overall water splitting, J. Colloid Interface Sci. 622 (2022) 250–260, https://doi.org/10.1016/j.jcis.2022.04.127.

[22] R.N. Wasalathanthri, S. Jeffrey, N. Su, K. Sun, D.M. Giolando, Stoichiometric control of electrocatalytic amorphous nickel phosphide to increase hydrogen evolution reaction activity and stability in acidic medium, ChemistrySelect 2 (2017) 8020–8027, https://doi.org/10.1002/slct.201701755.

[23] W. Jo, D. Jeong, J. Jeong, T. Kim, S. Han, M. Son, Y. Kim, Y.H. Park, H. Jung, Electrocatalytic properties of pulse-reverse electrodeposited nickel phosphide for hydrogen evolution reaction, Front. Chem. 9 (2021), https://doi.org/10.3389/fchem.2021.781838.

[24] J. Zhang, X. Cao, M. Guo, H. Wang, M. Saunders, Y. Xiang, S.P. Jiang, S. Lu, Unique Ni crystalline core/Ni phosphide amorphous shell heterostructured electrocatalyst for hydrazine oxidation reaction of fuel cells, ACS Appl. Mater. Interface. 11 (2019) 19048–19055, https://doi.org/10.1021/acsami.9b00878.

[25] J. Hu, L. Peng, A. Primo, J. Albero, H. García, High-current water electrolysis performance of metal phosphides grafted on porous 3D N-doped graphene prepared without using phosphine, Cell Rep. Phys. Sci. 3 (2022), https://doi.org/10.1016/j.xcrp.2022.100873.

[26] L. Yu, H. Zhou, J. Sun, I.K. Mishra, D. Luo, F. Yu, Y. Yu, S. Chen, Z. Ren, Amorphous NiFe layered double hydroxide nanosheets decorated on 3D nickel phosphide nanoarrays: a hierarchical core-shell electrocatalyst for efficient oxygen evolution, J. Mater. Chem. A Mater. 6 (2018) 13619–13623, https://doi.org/10.1039/c8ta02967a.

[27] S.M. Pawar, A.T. Aqueel Ahmed, C.H. Lee, P.T. Babar, J.H. Kim, S.U. Lee, H. Kim, H. Im, Experimental and theoretical insights into transition-metal (Mo, Fe) codoping in a bifunctional nickel phosphide microsphere catalyst for enhanced overall water splitting, ACS Appl. Energy Mater. 4 (2021) 14169–14179, https://doi.org/10.1021/acsaem.1c02930.

[28] S. Liu, Y. Xu, C. Wang, Y. An, Metal-organic framework derived Ni2P/C hollow microspheres as battery-type electrodes for battery-supercapacitor hybrids, ChemElectroChem 6 (2019) 5511–5518, https://doi.org/10.1002/celc.201901504.

[29] S. Farokhi, M. Roushani, H. Hosseini, Advanced core-shell nanostructures based on porous NiCo-P nanodiscs shelled with NiCo-LDH nanosheets as a high-performance electrochemical sensing platform, Electrochim. Acta 362 (2020), 137218, https://doi.org/10.1016/j.electacta.2020.137218.

[30] R. Bernasconi, M.I. Khalil, C. Iaquinta, C. Lenardi, L. Nobili, L. Magagnin, Nickel phosphides fabricated through a codeposition–annealing technique as low-cost electrocatalytic layers for efficient hydrogen evolution reaction, ACS Appl. Energy Mater. 3 (2020) 6525–6535, https://doi.org/10.1021/acsaem.0c00733.

[31] Z.X. Cai, X.H. Song, Y.R. Wang, X. Chen, Electrodeposition-assisted synthesis of Ni2P nanosheets on 3D graphene/Ni foam electrode and its performance for electrocatalytic hydrogen production, ChemElectroChem 2 (2015) 1665–1671, https://doi.org/10.1002/celc.201500239.

[32] L. Chai, S. Liu, S. Pei, C. Wang, Electrodeposited amorphous cobalt-nickel-phosphide-derived films as catalysts for electrochemical overall water splitting, Chem. Eng. J. 420 (2021), 129686, https://doi.org/10.1016/j.cej.2021.129686.

[33] S. Wang, L. Zhang, X. Li, C. Li, R. Zhang, Y. Zhang, H. Zhu, Sponge-like nickel phosphide–carbon nanotube hybrid electrodes for efficient hydrogen evolution over a wide pH range, Nano Res. 10 (2017) 415–425, https://doi.org/10.1007/s12274-016-1301-9.

[34] X. Yu, Z.Y. Yu, X.L. Zhang, Y.R. Zheng, Y. Duan, Q. Gao, R. Wu, B. Sun, M.R. Gao, G. Wang, S.H. Yu, "superaerophobic" nickel phosphide nanoarray catalyst for efficient hydrogen evolution at ultrahigh current densities, J. Am. Chem. Soc. 141 (2019) 7537–7543, https://doi.org/10.1021/jacs.9b02527.

[35] A. Lasia, Mechanism and kinetics of the hydrogen evolution reaction, Int. J. Hydrogen Energy 44 (2019) 19484–19518, https://doi.org/10.1016/J.IJHYDENE.2019.05.183.

[36] C. Liu, T. Gong, J. Zhang, X. Zheng, J. Mao, H. Liu, Y. Li, Q. Hao, Engineering Ni_2P–$NiSe_2$ heterostructure interface for highly efficient alkaline hydrogen evolution, Appl. Catal. B 262 (2020), 118245, https://doi.org/10.1016/J.APCATB.2019.118245.

[37] S. Anantharaj, S. Noda, V.R. Jothi, S.C. Yi, M. Driess, P.W. Menezes, Strategies and perspectives to catch the missing pieces in energy-efficient hydrogen evolution reaction in alkaline media, Angew. Chem. Int. Ed. 60 (2021) 18981–19006, https://doi.org/10.1002/ANIE.202015738.

[38] M.M. Alsabban, M.K. Eswaran, K. Peramaiah, W. Wahyudi, X. Yang, V. Ramalingam, M.N. Hedhili, X. Miao, U. Schwingenschlögl, L.J. Li, V. Tung, K. W. Huang, Unusual activity of rationally designed cobalt phosphide/oxide heterostructure composite for hydrogen production in alkaline medium, ACS Nano 16 (2022) 3906–3916, https://doi.org/10.1021/acsnano.1c09254.

[39] F.L. Wang, Y.N. Zhou, J.Y. Lv, B. Dong, X.Y. Zhang, W.L. Yu, J.Q. Chi, Z.X. Wu, L. Wang, Y.M. Chai, Nickel hydroxide armour promoted CoP nanowires for alkaline hydrogen evolution at large current density, Int. J. Hydrogen Energy 47 (2022) 1016–1025, https://doi.org/10.1016/J.IJHYDENE.2021.10.117.

[40] P.F. Liu, S. Yang, B. Zhang, H.G. Yang, Defect-rich ultrathin cobalt-iron layered double hydroxide for electrochemical overall water splitting, ACS Appl. Mater. Interface. 8 (2016) 34474–34481, https://doi.org/10.1021/ACSAMI.6B12803.

[41] A. Shahroudi, M. Esfandiari, S. Habibzadeh, Nickel sulfide and phosphide electrocatalysts for hydrogen evolution reaction: challenges and future perspectives, RSC Adv. 12 (2022) 29440–29468, https://doi.org/10.1039/d2ra04897c.

[42] L. Fang, Y. Xie, Y. Yang, B. Zhu, Y. Wang, M. Liu, K. Zhao, H. Zhao, J. Zhang, Interfacial electronic modulation of multishelled CoP hollow spheres via surface reconstruction for high-efficient hydrogen evolution reaction, ACS Appl. Energy Mater. 3 (2020) 309–318, https://doi.org/10.1021/acsaem.9b01562.

[43] Y. Huang, L. Hu, R. Liu, Y. Hu, T. Xiong, W. Qiu, M.S. (Jie T.) Balogun, A. Pan, Y. Tong, Nitrogen treatment generates tunable nanohybridization of Ni_5P_4 nanosheets with nickel hydr(oxy)oxides for efficient hydrogen production in alkaline, seawater and acidic media, Appl. Catal. B 251 (2019) 181–194, https://doi.org/10.1016/j.apcatb.2019.03.037.

[44] J. Zhou, C. Huang, Q. Zhou, Y. Xie, L. Yang, L. Yu, Y. Yu, Electronic structure regulation of nickel phosphide for efficient overall water splitting, Inorg. Chem. 61 (2022) 9318–9327, https://doi.org/10.1021/ACS.INORGCHEM.2C01070.

[45] Y. Wang, L. Liu, X. Zhang, F. Yan, C. Zhu, Y. Chen, Self-supported tripod-like nickel phosphide nanowire arrays for hydrogen evolution, J. Mater. Chem. A Mater. 7 (2019) 22412–22419, https://doi.org/10.1039/C9TA07859B.

[46] J. Li, W. Xu, D. Zhou, J. Luo, D. Zhang, P. Xu, L. Wei, D. Yuan, Synthesis of 3D flower-like cobalt nickel phosphate grown on Ni foam as an excellent electrocatalyst for the oxygen evolution reaction, J. Mater. Sci. 53 (2018) 2077–2086, https://doi.org/10.1007/s10853-017-1631-3.

[47] J. Duan, S. Chen, C.A. Ortíz-Ledón, M. Jaroniec, S.Z. Qiao, Phosphorus vacancies that boost electrocatalytic hydrogen evolution by two orders of magnitude, Angewan. Chemie - Int. Ed. 59 (2020) 8181–8186, https://doi.org/10.1002/anie.201914967.

[48] Z. Zhou, Z. Pei, L. Wei, S. Zhao, X. Jian, Y. Chen, Electrocatalytic hydrogen evolution under neutral pH conditions: current understandings, recent advances, and future prospects, Energy Environ. Sci. 13 (2020) 3185–3206, https://doi.org/10.1039/d0ee01856b.

[49] F. Sun, Q. Tang, D. Jiang, Theoretical advances in understanding and designing the active sites for hydrogen evolution reaction, ACS Catal. 12 (2022) 8404–8433, https://doi.org/10.1021/acscatal.2c02081.